The International Journal of Advanced Manufacturing Technology (2019) 102:1839–1852
https://doi.org/10.1007/s00170-018-03229-1

ORIGINAL ARTICLE

Gaussian process regression to predict the morphology of friction-stir-welded aluminum/copper lap joints

M. Krutzlinger[1] · E. Meltzer[1] · M. Muehlegg[2] · M. F. Zaeh[1]

Received: 23 August 2018 / Accepted: 14 December 2018 / Published online: 14 January 2019

Abstract
The joining of materials with different or even competing properties is of high industrial interest regarding resource-efficient production. Friction stir welding (FSW) has been employed to create high-quality joints of dissimilar material combinations. Many studies report both metallurgical bonding and form-fit to be the relevant joining mechanisms. While metallurgical bonding is driven by interdiffusion and occurs in almost every case, form-fit can only appear if the interface is deformed. The hooks of the deformed interface cause interlocking; however, they also result in an increased stress concentration. Hence, the hooking can either enhance or reduce the joint strength depending on their geometries. This study demonstrates an approach to predict the morphology of the cross-sectional interfacial area of friction-stir-welded multi-material joints. Image processing was used to convert cross sections of aluminum/copper lap joints into binary b/w images. Using Gaussian process regression, a data-driven model of the interfacial area's morphology was constructed based on 13 data sets. The applicability of the resulting Gaussian process model was tested for seven data sets by comparing the algorithm's morphological predictions with cross sections welded with test parameters that were not used for training. This allows to estimate, which joining mechanism is relevant or dominant for the overall joint strength. The predicted results agreed well with the actual cross sections. Recesses as well as hooks at the interfacial area were successfully predicted even for a limited number of training data. To enhance the space of possible uses of the model for subsequent applications (e.g., simulation of fracture mechanics), more input parameters can be implemented into the model.

Keywords Friction stir welding · Gaussian process regression · Dissimilar materials · Image processing · Aluminum/copper lap joints

1 Introduction

Welding dissimilar material combinations is very challenging due to the different, sometimes competing, properties of the materials [1]. When using fusion welding processes, such as arc welding, the distinct formation of intermetallic compounds (IMCs) can negatively influence the properties of dissimilar joints [2]. Friction stir welding (FSW) has proven to be suitable for joining combinations of dissimilar materials [3]. Since FSW is a solid-state welding process, joints with a minimal amount of IMCs can be produced. The amount of IMCs can be further reduced by modified FSW processes (e.g., ultrasound-enhanced FSW [4, 5]).

✉ M. Krutzlinger
markus.krutzlinger@tum.de

Extended author information available on the last page of the article.

Numerous studies proved a strong correlation between the welding parameters, the morphology of the interfacial area, and the characteristics of dissimilar material joints. However, a model to predict the morphology as a result of the welding parameters has not been developed: this is the aim of this study. In the following, an overview of the most influential welding conditions for the interface morphology will be given for the most common material combinations aluminum/steel, aluminum/titanium, and aluminum/copper. Similar observations were also reported for dissimilar joints of aluminum and magnesium [6–9] and of aluminum and steel [10].

1.1 Influences on the morphology of the interfacial area - general overview

The welding conditions highly influence the joint properties, which result from the IMC formation and the shape of the interfacial areas for numerous dissimilar material

joints. The morphology of the interfacial area is crucial for the resulting joining mechanisms. If neither intermixing of the materials nor deformation of the interfacial area occurs, joining is achieved exclusively by metallurgical bonding. A deformation of the interfacial area causes an enlarged joining area, which enhances metallurgical bonding on the one hand. On the other hand, the deformation enables form-fit, which may support metallurgical bonding and increase the overall strength of joints. The friction stir dovetailing (FSD) aims to achieve an ideal combination of mechanical interlocking and metallurgical bonding [11, 12]. However, for lap joints, an unsuitable deformation reduces the joint strength by magnifying the stress concentration and reducing of the upper sheet's thickness. This was first reported as the "hooking effect" for dissimilar aluminum/aluminum joints [13]. Reducing the deformation of the lower material into the upper material by using a concave probe-tip design results in an enhanced fatigue performance [14]. In the following, a brief overview of the influence of welding parameters on the interfacial area (and the correlating joint properties) for several friction-stir-welded dissimilar material combinations is given.

Applying laser-assisted FSW (LAFSW) of aluminum AA 5182 with steel ZStE340 in butt-joint configuration was conducted in [15]. The authors observed a saw tooth-shaped interfacial area and concluded that both mechanical interlocking and metallurgical bonding were effective joining mechanisms. The high shear strain and frictional heating during FSW of aluminum AA6181-T4 with the steels DP600 and HC260LA HSS in butt-joint configuration caused the formation of IMCs and mechanical interlocking of both materials on a microscopic scale [16]. The properties of lap joints of aluminum Al 5054 and steel DP600 also significantly depended on the tool penetration depths into the lower steel sheet [17]. Restricting the material flow to the steel sheet inhibited mechanical interlocking and resulted in diffusion-based joining. A substantial increase of the joint strength was observed for penetration depths of about 0.2 mm, for which mechanical interlocking occurred at the edges of the interfacial area.

Swirl-like structures at the interfacial area were reported for butt joints of aluminum AA 2024-T3 and titanium TiAl6V4 [18]. These structures were believed to strengthen the joint by allowing for local micro-mechanical and metallurgical bonding. Similar observations were described in [19] for lap joints of aluminum ADC12 and pure titanium. Almost identical joint strengths were reported for lap joints of aluminum LF6 with titanium TC1, despite the tested samples had very different interface structures: on the one side, a highly intermixed interfacial area, and on the other side, an interfacial area with almost no deformation of the lower titanium sheet [20, 21]. Similar results were observed for varying the distance from the probe tip to the interface and the rotational speed for joints of two combinations of aluminum and titanium in lap-joint configuration [22]. The highest joint strength was achieved when the probe tip was close to, but not penetrating the titanium surface for lap joints of aluminum AA 6060 and titanium Ti6Al4V [23]. In this case, no deformation of the interfacial area was observed and the joining was based on a very thin IMC layer. If the probe was plunged deeper into the titanium sheet, the interfacial area was macroscopically deformed. Although this could have provided additional form-fit, the joint strength was reduced. The formation of IMCs at the interfacial area was concluded to be also the primary joining mechanism for butt joints of aluminum AA 6061 and titanium Ti6Al4V [24].

1.2 Influences on the morphology of the interfacial area – aluminum/copper joints

Offsetting the probe relative to the butt-joint interface of aluminum AA 6082-T6 and copper-DHP (R 240) strongly influenced the morphology of the interfacial area [25]. However, no effect on the mechanical properties of the joints was observed since increasing the tool offset caused a reduction in IMC formation and also stirred copper particles with a sharp geometry into the aluminum matrix, which led to metallurgical discontinuities. A tunnel defect was reported for butt joints of AA 1060 and commercially pure copper when the copper sheet was positioned on the retreating side [26]. A copper hook, which was stirred into the aluminum matrix and was thought to possibly provide additional mechanical bonding, was detected in cross sections of butt-joined aluminum AA 2024 and copper Cu10100 [27]. The material flow in lap joints of aluminum AA 1060 and commercially pure copper caused a movement of the interface into the lower sheet [28]. The resulting interface morphology was asymmetrical and cavities were observed for increasing feed rates. Experiments with varying probe lengths for aluminum EN AW-1050 H14 and copper EN CW024A R240 in lap-joint configuration were conducted by [29]. The cross sections showed no deformation of the interfacial area for the lowest probe length. A deformed yet sound interfacial area with little hooking was observed for medium probe lengths. The highest probe lengths led to severe hooking and cavities. The maximum joint strength was measured when the copper sheet was only minimally penetrated. Detailed analyses of the microstructure and the IMC formation, which are not the focus of this study, are discussed, e.g., in [30–34] for butt joints and in [35, 36] for lap joints of aluminum and copper. A review on FSW of aluminum and copper was presented in [37].

1.3 Key findings of the discussed literature – relevance of the considered approach

The following conclusions can be drawn from the studies mentioned above:

1. The morphology of the interfacial area is dependent on the welding conditions and strongly influences, which joining mechanism is present and promoted.
2. Metallurgical bonding by interdiffusion is always present and enhanced by an enlarged interfacial area.
3. Mechanical bonding by form-fit may occur as well and can result in either an increase or a decrease in joint strength, depending on the welding conditions.

Several approaches have been discussed to estimate the formation and thickness of IMC layers, e.g., for aluminum/titanium joints [22, 23] and aluminum/copper joints [38–41], as well as to control the thickness of the layers [42]. As mentioned above, a prediction of the morphology of the interfacial area of friction-stir-welded dissimilar joints, which strongly influences metallurgical and mechanical bonding, has not yet been presented. The use of analytical or numerical models is quite difficult due to the high complexity of the proposed task. Because of this, in this study a data-driven Gaussian process (GP) is used to predict the interface morphology. GP regression (GPR) has already been used to model complex processes, such as nonlinear systems [43] or dynamic systems [44], and dependencies of welding processes [45–47]. It was proven that GPR models can be used for real-time-prediction applications.

2 Materials and methods

This section provides information on the approach for the prediction of the interface morphology in friction-stir-welded dissimilar aluminum/copper lap joints. After giving an overview on the chosen approach, the image processing workflow used to prepare the cross-section images as training data and the procedure of GPR will be discussed.

2.1 Approach

Figure 1 shows the cross section of a friction-stir-welded aluminum/copper lap joint. As can be seen, the copper sheet was deformed and hooks occurred on both sides of the stirred area. The morphology of the interfacial area can be identified clearly, if the image is converted into black and white (b/w) space, where black corresponds to 0 (aluminum) and white to 1 (copper), and copper particles within the aluminum matrix are "filled" with aluminum. It is evident that the morphology is not continuously differentiable and cannot be modeled directly (e.g., via linear polynomial fitting).

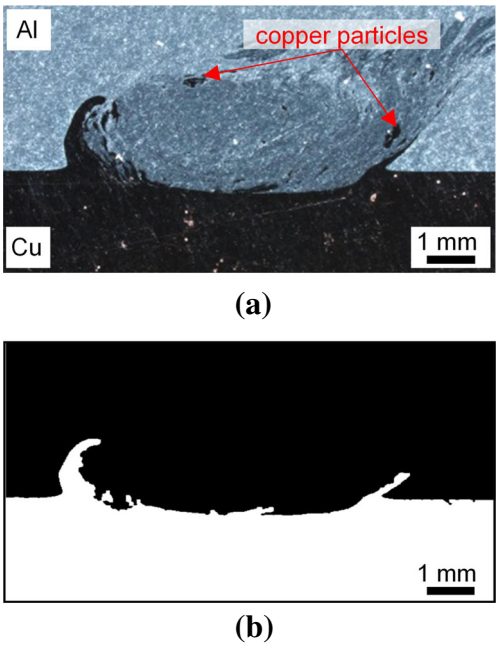

Fig. 1 Exemplary cross section of a joint with hooks at the interfacial area (**a**) and the corresponding binarized image (**b**)

The b/w image can also be interpreted as a 3D matrix with the dimensions of (1) image width (x-coordinate), (2) image height (y-coordinate) and (3) color values ranging from 0 to 1 (z-coordinate). Each pixel has a defined x- and y-coordinate and a color value, which can be described by its dependency on the welding parameters by scattering the image. The input values for modeling are the welding parameters (rotational speed, feed rate, and probe-tip-to-interface distance before welding) of each pixel. The output values are the predicted color values of the pixels. In the following, vectors are represented by bold letters and matrices by capital letters. A model is considered to describe the dependency between the welding parameters and each pixel value. The model consists of a linear combination of weights $\boldsymbol{w}$ and nonlinear basis functions $\boldsymbol{\phi}(\boldsymbol{x})$, such that

$$y = f(\boldsymbol{x}) + \epsilon = \boldsymbol{w}^T \boldsymbol{\phi}(\boldsymbol{x}) + \epsilon. \tag{1}$$

Here, y is the output value of one pixel (color value), $\boldsymbol{x}$ the vector of the input values (welding parameters), $\epsilon \sim N(0, \sigma_n^2)$ the vector of random noise (normal distribution, represented by $N()$) with zero-mean and variance σ_n^2 and $\boldsymbol{w}$ is a vector of parameters (coefficients) of the linear model. By placing a probability distribution on the parameters $\boldsymbol{w}$, $f(\boldsymbol{x}) = \boldsymbol{w}^T \boldsymbol{\phi}(\boldsymbol{x})$ forms a GP. Often, this prior distribution is chosen to be a zero-mean Gaussian prior with covariance Σ_p such that $\boldsymbol{w} \sim N(0, \Sigma_p)$. The aim of GPR [48] is then

to infer the parameters $\boldsymbol{w}$ from measured data pairs $(\boldsymbol{x}, y)$. GPs provide numerous advantages over other models:

- The parameters $\boldsymbol{w}$ are assumed to be distributed and therefore allow for the introduction of uncertainty as well as statistical dependencies into the model.
- Compared to various other machine learning approaches, such as, e.g., deep neural networks [49], GPs only require a small amount of data.
- Evaluating a GP model not only results in the expected model output y but also provides a confidence interval.
- The inference on data with Gaussian likelihood is fast and tractable.

In order to achieve a convenient input-output mapping, the following approach was performed in this study by applying GPs:

1. Conversion of the cross sections into b/w color space via image processing. This conversion also reduced the complexity of the model.
2. Development of an algorithm based on GPs, which can correlate welding parameters (rotational speed, feed rate, and probe-tip-to-interface distance before welding) with the color value of each pixel of an actual (and virtual) cross section. Evaluating a GP model also provides information on the variance of each pixel's color leading to a greyscale image, which could also be interpreted.
3. Training of the prediction algorithm with converted images of the cross sections from 13 joints, which were welded with different parameter settings.
4. Validation of the algorithm by predicting the cross-sectional images with 7 welding parameter settings, which were not used for training.

2.2 Implementation

The image processing was performed using several pre-implemented functions of the MathWorks MATLAB environment. Figure 2 shows the workflow of the image processing algorithm. The images of the cross sections (a) are converted into a greyscale space (b). To reduce the color complexity a further conversion into b/w color space is applied (c). A threshold of 0.367 for interpreting greyscale values as black or white showed the highest accuracy. The pixels' color values are then inverted to identify the

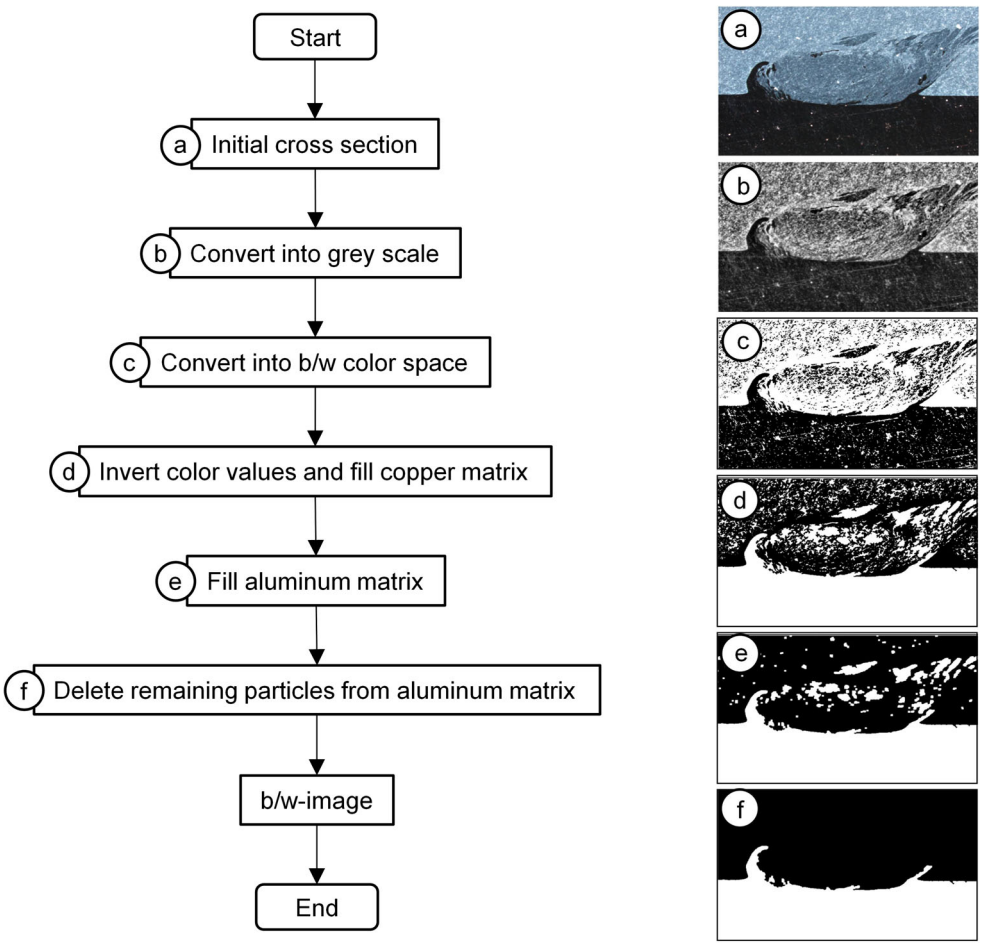

Fig. 2 Workflow diagram of image processing to convert cross-section images into b/w color space

boundary of the copper sheet's area and fill it more efficiently (d). White areas within the aluminum sheet with a radius of less than 3 pixels are "opened" (and filled consequently) (f). For this study, the complexity of the b/w images used to train the GP was further reduced by removing undefined areas or areas representing copper particles. To do this, all areas made up with fewer white pixels than the largest area (i.e., the copper sheet) were also replaced with black pixels (g). However, copper particles could also be predicted in further studies by improving the image processing algorithm.

2.3 Basics of Gaussian process regression

As already mentioned, the application of GPs for stochastic modeling and machine learning tasks has been gaining in popularity. A probability distribution of functions can be defined by GPs. Therefore, models developed using GPR provide not only the best function for matching input and output data, but also allow for a probability distribution over likely functions [50]. A brief introduction on the essentials of GPR, as used for this study, will be given in the following and is based on [51], where more detailed explanations can be found. Note that X_h is the design matrix of all column vector inputs $\boldsymbol{x}_h$ for the total set of training data $D_h = (X_h, \boldsymbol{y}_h)$. In this study, $\boldsymbol{x}_h$ will provide the information of the rotational speed, the feed rate, and the probe-tip-to-interface distance of each experiment. Therefore, X_h will contain the parameter triples of $\boldsymbol{x}_h$ in its columns. The index "h" marks training data ("historical") to enhance readability. The posterior distribution $p(\boldsymbol{w}|\boldsymbol{y}_h, X_h)$ for p data pairs $(\boldsymbol{x}, y)$ is described by Bayes' theorem:

$$p(\boldsymbol{w}|\boldsymbol{y}_h, X_h) = \frac{p(\boldsymbol{y}_h|X_h, \boldsymbol{w}) \cdot p(\boldsymbol{w})}{p(\boldsymbol{y}_h|X_h)}. \tag{2}$$

It is an updated belief of the parameter values $\boldsymbol{w}$ based on the input data X_h and on the output data $\boldsymbol{y}_h$. The prior belief for the model parameters is denoted by $p(\boldsymbol{w})$. In this study, a zero-mean Gaussian distribution with covariance Σ_p such that $p(\boldsymbol{w}) = N(0, \Sigma_p)$ is assumed. Based on the input X_h and the prior parameters $\boldsymbol{w}$, the likelihood of the output $\boldsymbol{y}_h$ is represented by $p(\boldsymbol{y}_h|X_h, \boldsymbol{w})$. Since ϵ in Eq. 1 is modeled as a normal distribution, the likelihood for all p data pairs is

$$p(\boldsymbol{y}_h|X_h, \boldsymbol{w}) = \frac{1}{(2\pi\sigma_n^2)^{\frac{p}{2}}} \cdot e^{-\left((\boldsymbol{y}_h \boldsymbol{w}^T \boldsymbol{\phi}(X_h)) \frac{1}{2\sigma_n^2} (\boldsymbol{y}_h \boldsymbol{w}^T \boldsymbol{\phi}(X_h))^T\right)}. \tag{3}$$

The so-called marginal likelihood $p(\boldsymbol{y}_h|X_h)$ is used for normalization. Since $p(\boldsymbol{w})$ and $p(\boldsymbol{y}_h|X_h, \boldsymbol{w})$ are normal, the normalization $p(\boldsymbol{y}_h|X_h, \boldsymbol{w})$ does not change the mean and the covariance of their product. Hence, it can be neglected for the calculation of the mean and the covariance of the posterior $p(\boldsymbol{w}|\boldsymbol{y}_h, X_h)$. To determine the distribution of the (predictive) posterior for the function value f_* at the test input $\boldsymbol{x}_*$, the joint distribution $p(f_*, \boldsymbol{w}|\boldsymbol{x}_*, \boldsymbol{y}_h, X_h)$ needs to be marginalized leading to the posterior predictive distribution

$$\begin{aligned} p(f_*|\boldsymbol{x}_*, \boldsymbol{y}_h, X_h) = & \\ & \int p(f_*, \boldsymbol{w}|\boldsymbol{x}_*, \boldsymbol{y}_h, X_h)\, d\boldsymbol{w} = \\ & \int p(f_*|\boldsymbol{x}_*, \boldsymbol{w}) \cdot p(\boldsymbol{w}|\boldsymbol{y}_h, X_h)\, d\boldsymbol{w}. \end{aligned} \tag{4}$$

The result for the function value f_* at the test input $\boldsymbol{x}_*$ then is

$$\begin{aligned} & p(f_*|\boldsymbol{x}_*, \boldsymbol{y}_h, X_h) = \\ & N(K(\boldsymbol{x}_*, X_h) \cdot [K(X_h, X_h) + \sigma_n^2 I]^{-1} \cdot \boldsymbol{y}_h^T, \\ & K(\boldsymbol{x}_*, \boldsymbol{x}_*) - K(\boldsymbol{x}_*, X_h) \cdot \\ & [K(X_h, X_h) + \sigma_n^2 I]^{-1} \cdot K(X_h, \boldsymbol{x}_*)). \end{aligned} \tag{5}$$

$K(X_h, X_h)$, $K(\boldsymbol{x}_*, X_h)$, $K(X_h, \boldsymbol{x}_*)$, and $K(\boldsymbol{x}_*, \boldsymbol{x}_*)$ are defined by $K(A, B) = \boldsymbol{\phi}(A)^T \Sigma_p \boldsymbol{\phi}(B)$ for the inputs A and B, where $K(\boldsymbol{x}_*, X_h) = K(X_h, \boldsymbol{x}_*)^T$. The posterior predictive mean can be extracted from Eq. 5 by

$$\overline{f_*} = K(\boldsymbol{x}_*, X_h) \cdot [K(X_h, X_h) + \sigma_n^2 I]^{-1} \cdot \boldsymbol{y}_h^T \tag{6}$$

and the posterior predictive covariance by

$$\begin{aligned} cov(f_*) = & K(\boldsymbol{x}_*, \boldsymbol{x}_*) - K(\boldsymbol{x}_*, X_h) \cdot \\ & [K(X_h, X_h) + \sigma_n^2 I]^{-1} \cdot K(X_h, \boldsymbol{x}_*). \end{aligned} \tag{7}$$

The dependencies between points are described by the covariance matrix $K(A, B)$. This matrix can be constructed using one of numerous kernel functions. In this study, the squared exponential (SE) kernel function was used given by

$$K(A, B) = \sigma_n^2 \cdot exp\left(-\frac{\|A - B\|}{2l^2}\right). \tag{8}$$

The bandwidth of the kernel l is a hyperparameter (as well as the variance σ_n^2), which has to be optimized to adjust the model of each pixel. A high dependency for spatially close points as well as an infinite differentiability and a "smooth" progress are exemplary advantages of the SE kernel function. Other commonly used kernels include, e.g., periodic or linear kernel functions [52].

2.4 Model construction

As mentioned above, the inference on the test input data was derived from the GP model to predict the color value of each pixel. Hence, the color value itself is solely dependent on the three welding input parameters rotational speed n, feed rate v, and distance between the probe tip and the interface before welding d. Figure 3 shows the workflow to determine a model with optimized hyperparameters.

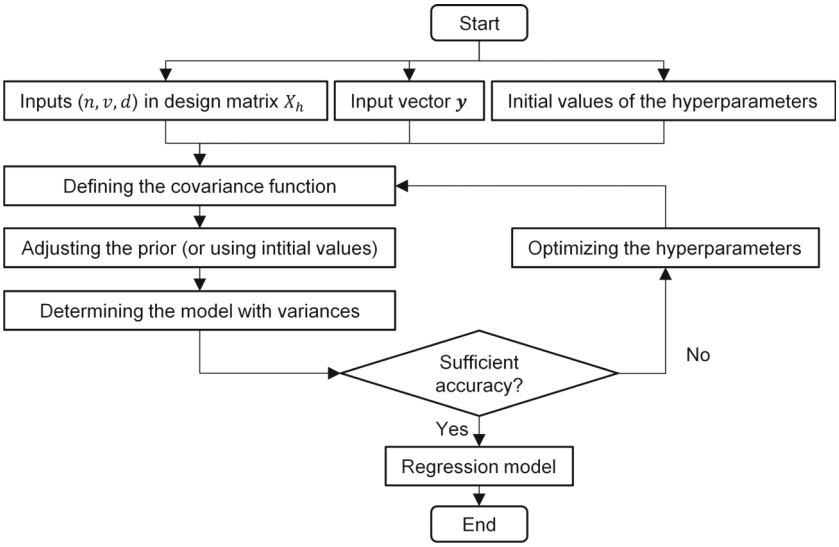

Fig. 3 Workflow to determine a model with optimized hyperparameters for each pixel

The input and output vectors as well as the initial values of the hyperparameters are used to build the covariance function of Eq. 8. Combined with a prior (estimated mean value) for a test input set $\boldsymbol{x}_*$ the predictive Gaussian output, consisting of the expected value and the standard deviation, can be derived. If the predicted results do not meet the actual pixels' values with sufficient accuracy, then the hyperparameters are optimized until the difference is minimized. Otherwise, the model for the pixel is complete.

For optimization of the hyperparameters, the negative logarithmic marginal likelihood from [51], which also provides a solution for a computer-based calculation, given by

$$\begin{aligned} &log(p(\boldsymbol{y}_h|X_h)) = \\ &-\frac{1}{2}\boldsymbol{y}_h^T[K(X_h, X_h) + \sigma_n^2 I]^{-1}\boldsymbol{y}_h \\ &-\frac{1}{2}log|K(X_h, X_h) + \sigma_n^2 I| - \frac{n}{2}log2\pi \end{aligned} \tag{9}$$

was minimized using the gradient-based Matlab function $fmincon()$. The initial value for both hyperparameters was 1 and 0.1 for the variance σ_n^2, which should account for the deviation of the actual pixels' color values in the experiments. The prior was defined with a believed mean value of 0 (so-called zero-mean prior), which addressed the assumption that the cross section consists only of aluminum, and consequently sets all pixels to be black. This prior assumption was adjusted by the algorithm and the probability of each pixel's color value to be 0 or 1 was derived.

2.5 Simplified task for model validation

The developed approach was validated for a simplified task regarding the accuracy of the model. A 3×3 matrix Z was defined for the simplified prediction task as

$$Z(x) = \begin{bmatrix} 1 & x^5 & 0 \\ 1-x & x & 1-x \\ 0 & 1-x & 0 \end{bmatrix} \tag{10}$$

for the training input vector

$$\boldsymbol{x} = \begin{pmatrix} 0.1 \\ 0.2 \\ \vdots \\ 0.9 \end{pmatrix} \tag{11}$$

This matrix was chosen arbitrarily since only values varying between 0 and 1 should result as to be expected for the afterward application. Another matrix meeting this condition would have been also suitable. In this simplified case, the columns of the design matrix are filled with the entries of the input vector (hence is the transposed input vector). The model was trained as described above and tested for the test input $\boldsymbol{x}_* = 0.65$, leading to the reference matrix

$$Z(0.65) = \begin{bmatrix} 1 & 0.116029 & 0 \\ 0.35 & 0.65 & 0.35 \\ 0 & 0.35 & 0 \end{bmatrix} \tag{12}$$

Comparing the entries of the reference and the prediction matrix

$$Z_*(0.65) = \begin{bmatrix} 1 & 0.1160 & 0 \\ 0.35 & 0.65 & 0.35 \\ 0 & 0.35 & 0 \end{bmatrix} \tag{13}$$

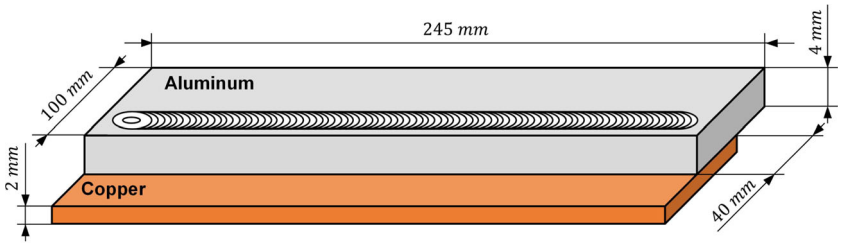

Fig. 4 Dimensions of the joint configuration

after training with the data of Eq. 11 shows that the model predicts them correctly at least to the fourth decimal place, which proves the validity of the approach. The hyper-parameters were adjusted automatically by the developed algorithm and may vary for each training process. The strong influence of the welding-parameter-related distance between the training and the test data points in normalized space was verified by applying test data points above 0.9. An increasingly insufficient quality of the predicted values was observed for test data points above 1.5.

3 Experimental results

Sheets of aluminum EN AW-1050 and copper CW008A in lap-joint configuration were friction-stir-welded on a Heller MCH 250 CNC milling machine. Both sheets were dimensioned to 245 × 100 *mm* with a thickness of 4 *mm* for aluminum (positioned on top, on the advancing side AS) and 2 *mm* for copper (positioned on the retreating side RS, see Fig. 4). The length of the weld seam was 215 *mm* and the overlap was set to 40 *mm* according to [39].

The tool consisted of a shoulder with diameter 14 *mm* and a conical probe with diameter 5 *mm*, which was manufactured with three equally distributed flats and a right-hand threading. The probe length was set with respect to the constant shoulder plunge depth of 0.1 *mm* and a constant tilt angle of 2° to ensure a defined probe-tip-to-interface distance in the position-controlled mode (see Fig. 5).

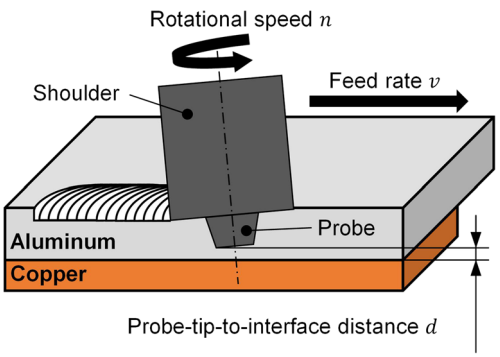

Fig. 5 Welding parameters rotational speed, feed rate, and probe-tip-to-interface distance

Table 1 lists the parameter sets for the rotational speed and the feed rate, as well as the distance between the probe tip and the interface before welding (positive values in the direction of the copper sheet), which were used for training. Furthermore, the averaged tensile shear forces of three specimens are given for each experiment. The specimens were located at distances of 62.5 *mm*, 122.5 *mm*, and 182.5 *mm* to the starting edge of the sheets and cut out perpendicular to the weld seam. The highest tensile shear force was achieved for very "hot" welding conditions (high ratio of rotational speed and feed rate) and a probe-tip positioned close to the interface. In contrast, a "cold" parameter set with a high distance between the probe tip and the interface caused the lowest joint strength.

The cross sections were also cut out perpendicular to the weld seam at a distance of 86 *mm* to the starting edge of the joints. Note that in the following scale bars of predicted cross sections are marked with a value set in brackets. As can be seen from Fig. 6, joints with different morphologies of the interfacial area were achieved. Hence, metallurgical as well as mechanical bonding should occur depending on the chosen parameter set. The lowest tensile shear force was measured for experiment 6, where a medium recess and

Table 1 Training data sets and measured tensile shear forces

Exp. no.	Rotational speed n in min^{-1}	Feed rate v in mm/min	Probe-tip-to-interface distance d in mm	Tensile shear force F_S in kN
1	800	100	−0.2	5.6
2	1800	100	−0.2	4.9
3	1800	300	−0.2	4.3
4	2800	300	−0.2	4.5
5	800	500	−0.2	2.8
6	800	100	0.0	3.7
7	1800	100	0.0	5.8
8	800	300	0.0	4.5
9	2800	300	0.0	5.2
10	2800	500	0.0	5.6
11	1800	100	0.2	5.1
12	1800	300	0.2	4.7
13	800	500	0.2	4.4

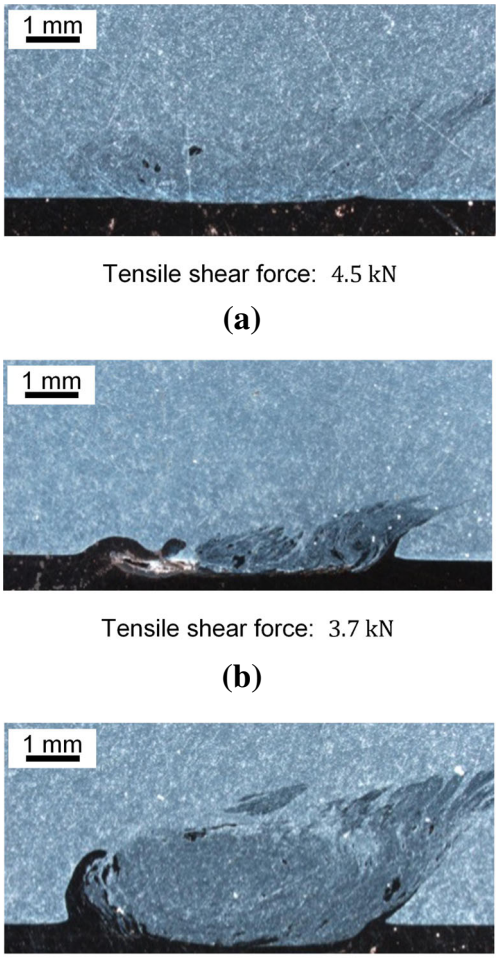

Fig. 6 Cross sections with different morphologies of the interfacial area and corresponding tensile shear forces for experiment 4 (**a**), experiment 6 (**b**), and experiment 9 (**c**)

little hooking occurred. The joint strength is increased for interfaces without hooking and almost no recessed copper sheet. Here, the joining is based on metallurgical bonding exclusively. Strong hooking in combination with a recess cause the highest achievable joint strength for experiment 9 with hooks slightly tilted away from the tool and processing area, respectively. The metallurgical bonding seems to be supported by a significant increase of possibilities for form-fit and therefore mechanical bonding. The according design matrix is

$$X_h = \begin{bmatrix} 800 & 1800 & \dots & 1800 & 800 \\ 100 & 100 & \dots & 300 & 500 \\ -0.2 & -0.2 & \dots & 0.2 & 0.2 \end{bmatrix} \quad (14)$$

4 Results and discussion

In this section, the prediction quality of the model regarding cross sections will be presented and discussed. The result for one test data point is analyzed in detail and a set of results is presented to evaluate the model's overall quality.

4.1 Detailed analysis of one cross section

After the simplified modeling task exhibited the high reliability of the developed approach, it was further tested on one cross section regarding the model's potential to predict the morphological characteristics of the interface. In the data set for the test data point, which will be discussed in the following, the parameters were set as follows: $n = 800\ min^{-1}$, $v = 500\ mm/min$ and $d = 0\ mm$ (parameter setting T5 in Table 2). This data point should be most heavily influenced by nearby training data points. The distance between the test data point and the i-th training data point was derived solving

$$\begin{aligned} distance^2 = &(n_{test} - n_{training,i})^2 \\ &+(v_{test} - v_{training,i})^2 \\ &+(d_{test} - d_{training,i})^2 \end{aligned} \quad (15)$$

Hence, the data points of the experiments 6–10, whose cross sections are shown in Fig. 7, should influence the test data points most, especially experiment 8 with the closest distance of 0.40.

The model provides greyscale images of the weighted overlays of the trained cross-sectional images for a proposed test data point (parameter set). Figure 8a shows the predicted cross section resulting from the expected value of each pixel. In the image displaying the expected values, the color values of the pixels are near 0 for aluminum in the upper part of the image and near 1 for copper at the bottom of the image. The position of the sheets is predicted correctly by the model. Furthermore, hooking can be expected for the test parameter set. The resulting image, after combining the expected value and the first positive standard deviation, which marks the upper boundary of the confidence interval, is shown in Fig. 8b. The positive first standard deviation was used to obtain the maximum difference to the pre-set prior belief (all pixels are aluminum; color value 0). The black and white areas of Fig. 8b explicitly define aluminum and copper areas, respectively. The grey areas indicate the likelihood of whether the pixel is black or white. An interface morphology with hooking should occur for 68% of all test samples. Summarizing, the result of Fig. 8a can be expected for the test parameter setting, but an increased hooking may also occur in 68% of all cases. In order to compare the trained cross sections and the model results more easily, the

Table 2 Test data sets and measured tensile shear forces

Exp. no.	Rotational speed	Feed rate	Probe-tip-to-interface distance	Tensile shear force
	n in min^{-1}	v in mm/min	d in mm	F_S in kN
T1	2800	100	−0.2	5.6
T2	1800	500	−0.2	3.8
T3	2800	500	−0.2	4.4
T4	1800	300	0.0	4.6
T5	800	500	0.0	4.1
T6	1800	500	0.0	4.0
T7	800	100	0.2	4.7

image of the expected values was binarized into the b/w color space, as illustrated in Fig. 9a. The actual cross section for the test data set is given in Fig. 9b. As can be seen, the predicted hooking was in good agreement with the actual cross section with regards to the height and volume of the copper hooks. Both cross sections also show a recess of the copper surface, which is more distinct in the predicted image. The pixels' color values of both cross sections revealed an agreement of 96% after converting the actual cross section into b/w color space. Hence, the fundamental aims of the presented modeling approach were achieved.

4.2 Overall predictive quality of the model

In total, seven (7) test parameter settings were used to evaluate the overall predictive quality of the developed model. Since regression models tend to result in a reduced quality at the boundaries of the used parameter range, a special emphasis was placed on the modeling of the boundary parameter sets (see Table 2). The resulting tensile shear forces of the experiments for the test data sets range from 3.8 kN to 5.6 kN, which is quite comparable to the training data sets and proves that they are suitable for testing the model quality. Again, the highest tensile shear force was

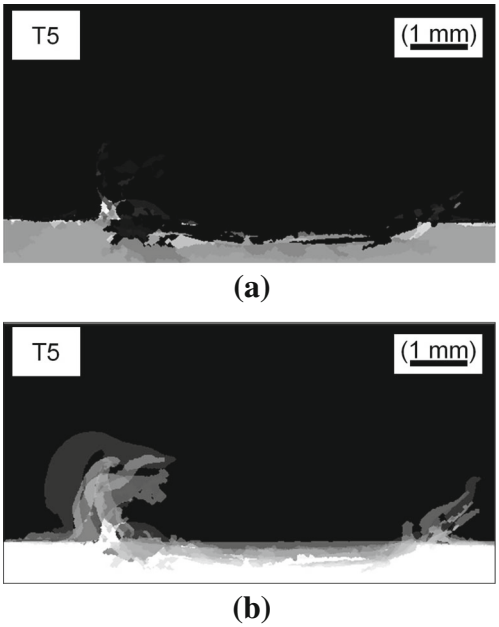

Fig. 8 Images of the expected values (**a**) and the first positive standard deviation (**b**) for the prediction of the test parameter setting T5: rotational speed $n = 800\ min^{-1}$, feed rate $v = 500\ mm/min$ and distance between the probe tip and the pre-welded interface area $d = 0mm$

measured for a data set causing tall hooks, which are tilted slightly away from the process zone (test data set T1). The lowest joint strength occurred for the data set T2, which results in an undefined morphology of the interfacial area.

Figure 10 shows the actual cross sections in the first column, the respective predicted images of the expected values in the second column and the predicted images of the first positive standard deviation in the third column.

The distinct morphologies prove that by using GPR the cross sections can be predicted with a high accuracy. The characteristic features in the images with expected values correlate well to the actual cross sections, especially for the parameter settings T1, T5 (as already discussed above), and T6. Although the hooking of the predicted expected

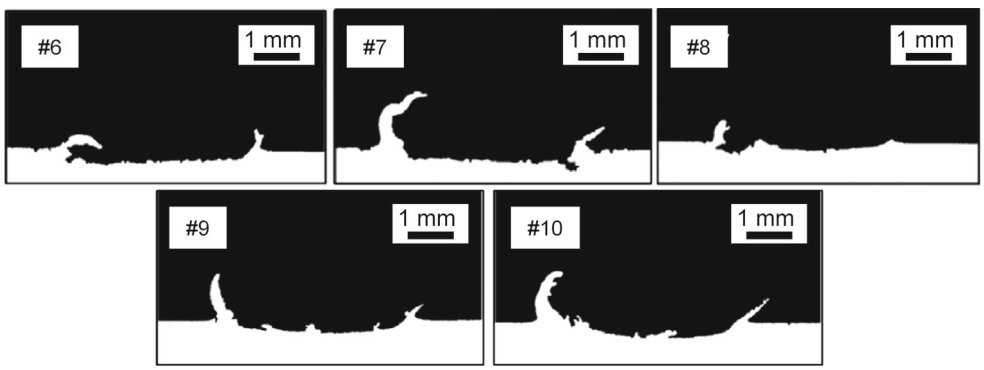

Fig. 7 Binarized images of cross sections for data points with the closest distance to the test parameter setting T5: rotational speed $n = 800\ min^{-1}$, feed rate $v = 500\ mm/min$ and distance between the probe tip and the pre-welded interface area $d = 0\ mm$

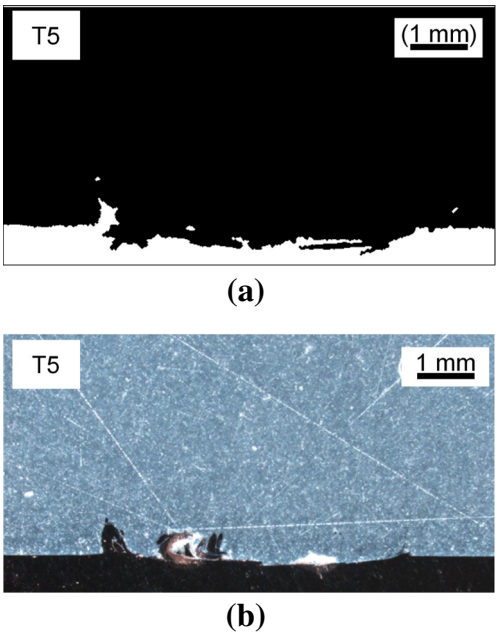

Fig. 9 Images of the predicted (**a**) and the actual (**b**) cross section for the test parameter setting T5: rotational speed $n = 800\ min^{-1}$, feed rate $v = 500\ mm/min$ and distance between the probe tip and the pre-welded interface area $d = 0\ mm$

value does not match the actual one perfectly, the first standard deviation already shows the typical characteristics of the morphology leading to high tensile shear forces. The results for the parameter settings T4 and T7 are also predicted very well, with the exception of the hooking on the left side. Recesses, which are not observed in the actual cross sections, are predicted by the model for the images of experiments T2 and T3. The first standard deviation of T2 implies that hooking may occur but is more unlikely than for T1. Since the actual and predicted cross sections of T2 and T3 are similar, the different joint strengths may result from the different welding conditions and the influence of metallurgical bonding, respectively. Almost no grey areas can be found for the predicted expected values and the predicted standard deviation of experiment T4. This results from T4 being the center point of the parameter space, where the model achieves the highest reliability for prediction. The images of the first positive standard deviation show a 68% probability for significant hooking for all parameter sets. Since the greyscale colors range from near black to near white, the threshold of the greyscale can significantly influence the interpretation of a given pixel as aluminum or copper. For example, a threshold level near 1 reduces the likelihood of misinterpreting copper as aluminum. However, the misinterpretation of possible copper pixels (greyscale values between 0 and threshold) is more likely. To this effect, the adaption of the threshold for the conversion from greyscale into b/w color space during image processing could be a suitable reference ($1 - 0.367$ due to inversion of b/w colors). An even more robust process to predict each pixel's value to be black or white can be achieved by increasing the input training data, which significantly reduces the overall variance of the model.

4.3 Use of the model in subsequent applications

As described in the previous sections, a strong cause and effect relationship between the welding conditions, the morphology of the interfacial area, and the resulting joint properties exists. The correlation between welding conditions and joint properties (e.g., the tensile shear strength) has already been discussed in numerous studies. The GPR could be adapted to generate substantial predictive results dealing with this topic by redefining and rearranging the model's in- and outputs and the workflow of the approach. However, the approach of this study describes the dependencies between the welding conditions and the morphology of the interface. The discussed results serve as a proof of concept of the model's applicability on this specific task. Several subsequent applications, which are part of future research, can possibly be derived from the developed model depending on the requested information:

- Shear loads on dissimilar joints cause stress concentration, delamination of (IMC) layers, and crack initiation as well as crack propagation at the interface. The morphology of the interface has a significant influence on the mode of the joint collapse. Fracture mechanics can be simulated, e.g., via cohesive zone models [53], which are based on a phenomenological point of view. Here, the morphology of the joint, which has to be simulated, is one of the most important inputs. The approach of this study enables to do an overall analysis of achievable joint strengths with limited experimental effort. As a consequence, identifying ideal welding conditions can be accelerated and the processing costs are reduced.
- Already existing welding processes can be modeled with the described approach and then be further optimized with respect to changed specifications of an application. For example, the processing time can be reduced by identifying the data set leading to a comparable morphology at a higher feed rate. Taking only the tensile shear force into account for modeling may also lead to a data set with similar joint strengths. However, the morphology of the interface remains concealed and undesired effects like stress concentration may occur. A combination of both approaches leads to the most valuable result.
- Several dissimilar material combinations like aluminum and titanium or aluminum and steel may cause severe tool wear, if the probe tip penetrates the lower material.

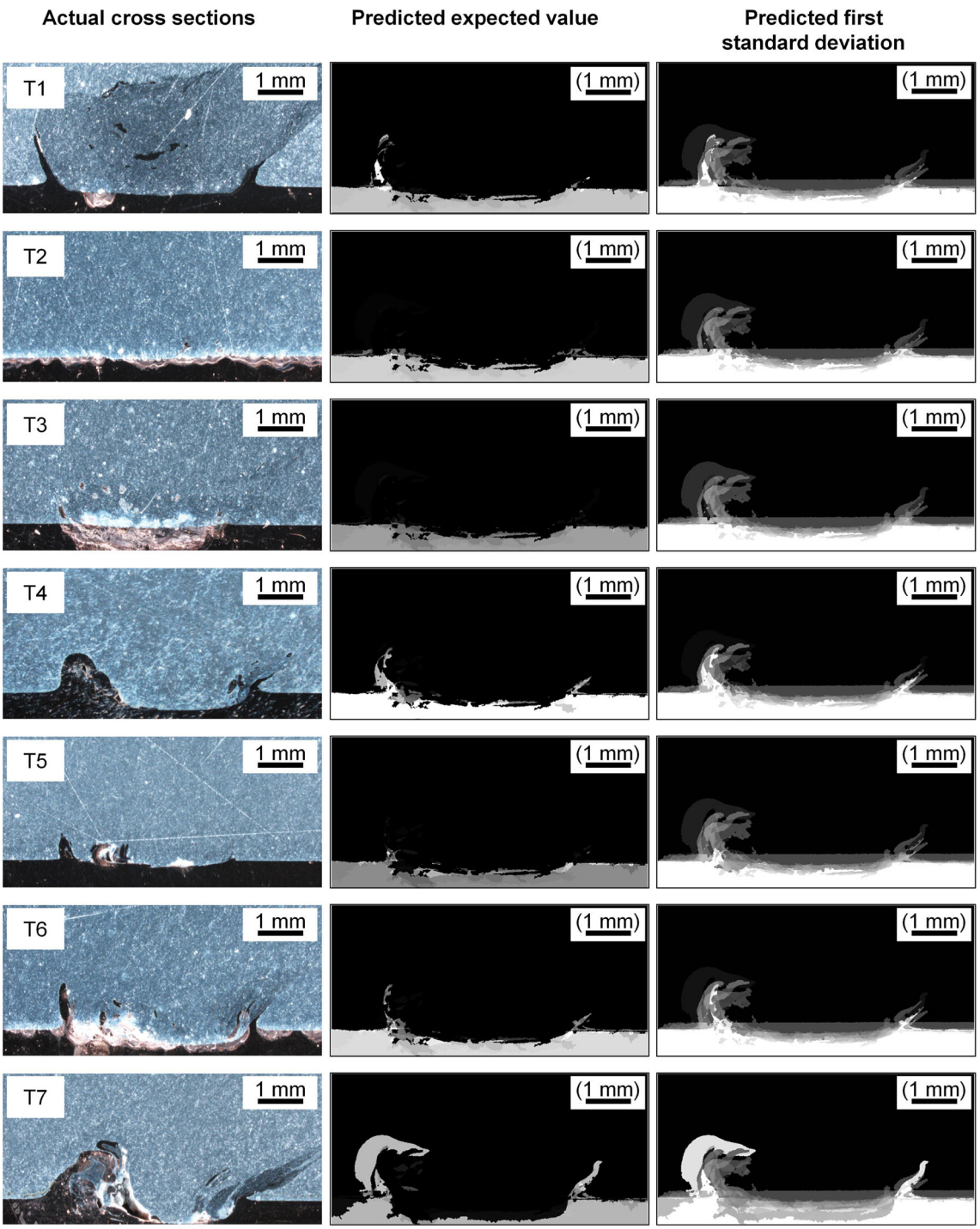

Fig. 10 Images of actual cross sections, expected values and first positive standard deviation for the test parameter settings

The approach of this study allows to identify a data set, where almost no recess occurs. Therefore, both an increase of the joint strength as well as a reduction of the experimental effort with cost intensive materials like titanium can be expected.

5 Improvements to the model

Although the model already shows a high accuracy to predict the cross sections, several improvements should be considered:

- The first challenge in accurately training the model is capturing suitable images. The training images have to be positioned accurately (in the same position) during image capture to ensure that the pre-welding interface and the rotational axis of the tool are congruent for all training images. Otherwise, the pixels' color values could be interpreted (and trained) incorrectly. Furthermore, it is vital that the metallographic cross sections do not contain any impurities, scratches and residues from polishing (e.g., for the experiments T2, T3, and T6). These may be interpreted incorrectly during image processing and negatively influence the training of the model.
- The image processing converts actual cross sections into b/w images. Hence, to identify the aluminum and copper areas precisely, it is crucial that the algorithm is adapted accurately to the characteristics of the actual cross sections, for example, regarding the threshold color values for the conversion from the greyscale to the b/w color space.
- The model quality can be improved by providing more data for training, including both further parameter settings as well as additional cross sections of parameter settings that were already used for training. This would significantly shrink the confidence interval.

6 Conclusions

In this study, the proof of concept for an innovative approach to predict the cross-sectional morphology of friction-stir-welded aluminum/copper lap joints using image processing and GPR was presented. A comparison of actual and predicted cross sections shows a high correlation regarding the welding-parameter-dependent characteristics (e.g., hooking, depth of recess), even for a limited number of data available for training. The described approach shows an efficient solution to customize the interfacial areas of friction-stir-welded dissimilar lap joints. The welding conditions can be tailored to distinct requirements without significant effort on time and costs for experiments and subsequent analysis of the cross sections. Since similar dependencies between welding conditions and interface morphologies have been reported for laser offset welding [54], the developed approach can also be applied to fusion welding technologies leading to a process-independent understanding of the influence of the interface morphology on the joint characteristics. Several options to further improve the quality of the predicted results were discussed. The robustness of the model can be increased by considering additional information to the input data. For example, the input vector could be extended to include material specifications, further material combinations or different workpiece dimensions. This would provide a large database to estimate joint characteristics without the need to conduct experiments. The resulting morphology of the cross-sectional interfacial area can be derived from the predicted images and included into FEM analysis to simulate shear tensile tests. Assuming time-dependent values for the welding parameters during processing, the model can be applied for use in online monitoring of the morphology of the interfacial area. Time-dependent values could include the rotational speed in temperature-controlled FSW or the pin-tip-to-interface distance in force-controlled FSW.

Acknowledgments The research project "Mechanisms in joining of dissimilar materials by friction stir welding" is part of the priority program 1640 (SPP1640) "Joining by plastic deformation," which is funded by the German Research Foundation (DFG). The authors would like to thank for the funding and the support. The authors would also like to thank Roland Marstatt from the Chair of Experimental Physics I of the University of Augsburg for the preparation of the cross sections, which were used in this study.

References

1. Kumar N, Yuan W, Mishra RS (2015) Friction stir welding of dissimilar alloys and materials. Butterworth-Heinemann (an imprint of Elsevier), Oxford, UK. 978-0-12-802418-8
2. Ben-Artzy A, Munitz A, Kohn G, Bronfin B, Shtechman A (2002) Joining of light hybrid constructions made of magnesium and aluminum alloys. TMS Annual Meeting: 295–302
3. Murr LE (2010) A review of FSW research on dissimilar metal and alloy systems. J Mater Eng Perform 19:1071–1089. https://doi.org/10.1007/s11665-010-9598-0
4. Strass B, Wagner G, Eifler D (2014) Realization of Al/Mg-Hybrid-Joints by ultrasound supported friction stir welding. Mater Sci Forum 783-786:1814–1819. https://doi.org/10.4028/www.scientific.net/MSF.783-786.1814
5. Thomae M, Wagner G, Strass B, Wolter B, Benfer S, Fuerbeth W (2018) Ultrasound enhanced friction stir welding of aluminum and steel. J Mater Sci & Technol 34:163–172. https://doi.org/10.1016/j.jmst.2017.10.022
6. Chen YC, Nakata K (2008) Friction stir lap joining aluminum and magnesium alloys. Scr Mater 58:433–436. https://doi.org/10.1016/j.scriptamat.2007.10.033
7. Firouzdor V, Kou S (2010) Al-to-Mg friction stir welding. Metall Mater Trans A 41:2914–2935. https://doi.org/10.1007/s11661-010-0340-1
8. Zettler R, da Silva AAM, Rodrigues S, Blanco A, dos Santos JF (2006) Dissimilar Al to Mg Alloy Friction Stir Welds. Adv Eng Mater 8:415–421. https://doi.org/10.1002/adem.200600030
9. Tan S, Zheng F, Chen J, Han J, Wu Y, Peng L (2017) Effects of process parameters on microstructure and mechanical properties of friction stir lap linear welded 6061 aluminum alloy to NZ30K magnesium alloy. J Magnes Alloy 5:56–63. https://doi.org/10.1016/j.jma.2016.11.005
10. Wei Y, Li J, Xiong J, Huang F, Zhang F (2012) Microstructures and mechanical properties of magnesium alloy and stainless steel weld-joint made by friction stir lap welding. Mater &Des 33:111–114. https://doi.org/10.1016/j.matdes.2011.07.016

11. Ross K, Whalen S, Reza-E-Rabby M, Hovanski Y (2017) US patent application No. 15/694,565: Systems and process for joining dissimilar materials and solid-state interlocking joint with intermetallic interface formed thereby. Battelle Memorial Institute
12. Reza-E-Rabby M, Ross K, Overman NR, Olszta MJ, McDonnell M, Whalen SA (2018) Joining thick section aluminum to steel with suppressed FeAl intermetallic formation via friction stir dovetailing. Scr Mater 148:63–67. https://doi.org/10.1016/j.scriptamat.2018.01.026
13. Cederqvist L, Reynolds AP (2000) Properties of friction stir welded aluminum lap joints. TWI Ltd., Cambridge
14. Ericsson M, Jin L, Sandstrom R (2007) Fatigue properties of friction stir overlap welds. Intern J Fatigue 29:57–68. https://doi.org/10.1016/j.ijfatigue.2006.02.052
15. Giera A, Merklein M, Baumeister P (2007) Laser-assisted friction stir welding of dissimilar steel and aluminum alloys. In: Proceedings of the 2nd ICNFT. Bremen, Germany, September 20–21. BIAS Verlag, Bremen, pp 421–430
16. Coelho RS, Kostka A, dos Santos JF, Kaysser-Pyzalla A (2012) Friction-stir dissimilar welding of aluminium alloy to high strength steels: Mechanical properties and their relation to microstructure. Mater Sci Eng: A 556:175–183. https://doi.org/10.1016/j.msea.2012.06.076
17. Shen Z, Chen Y, Haghshenas M, Gerlich AP (2015) Role of welding parameters on interfacial bonding in dissimilar steel/aluminum friction stir welds. Inter J Eng Sci Technol 18:270–277. https://doi.org/10.1016/j.jestch.2014.12.008
18. Dressler U, Biallas G, Alfaro Mercado U (2009) Friction stir welding of titanium alloy TiAl6V4 to aluminium alloy AA2024-T3. Mater Sci Eng: A 526:113–117. https://doi.org/10.1016/j.msea.2009.07.006
19. Chen YC, Nakata K (2009) Microstructural characterization and mechanical properties in friction stir welding of aluminum and titanium dissimilar alloys. Mater & Des 30:469–474. https://doi.org/10.1016/j.matdes.2008.06.008
20. Chen Y, Liu C, Liu G (2011) Study on the joining of titanium and aluminum dissimilar alloys by friction stir welding. Open Mater Sci J 5:256–261
21. Chen Y-H, Ni Q, Ke L-M (2012) Interface characteristic of friction stir welding lap joints of Ti/Al dissimilar alloys. Trans Nonferrous Met Soc China 22:299–304. https://doi.org/10.1016/S1003-6326(11)61174-6
22. Krutzlinger M, Marstatt R, Suenger S, Luderschmid J, Zaeh MF, Haider F (2014) Formation of joining mechanisms in friction stir welded dissimilar Al-Ti lap joints. Adv Mater Res 966–967:510–520. https://doi.org/10.4028/www.scientific.net/AMR.966-967.510
23. Chen ZW, Yazdanian S (2015) Microstructures in interface region and mechanical behaviours of friction stir lap Al6060 to Ti–6Al–4V welds. Mater Sci Eng: A 634:37–45. https://doi.org/10.1016/j.msea.2015.03.017
24. Song Z, Nakata K, Wu A, Liao J, Zhou L (2014) Influence of probe offset distance on interfacial microstructure and mechanical properties of friction stir butt welded joint of Ti6Al4V and A6061 dissimilar alloys. Mater & Des 57:269–278. https://doi.org/10.1016/j.matdes.2013.12.040
25. Galvão I, Loureiro A, Verdera D, Gesto D, Rodrigues DM (2012) Influence of tool offsetting on the structure and morphology of dissimilar aluminum to copper friction-stir welds. Metall Mater Trans A 43:5096–5105. https://doi.org/10.1007/s11661-012-1351-x
26. Xue P, Ni DR, Wang D, Xiao BL, Ma ZY (2011) Effect of friction stir welding parameters on the microstructure and mechanical properties of the dissimilar Al–Cu joints. Mater Sci Eng A 528:4683–4689. https://doi.org/10.1016/j.msea.2011.02.067
27. Carlone P, Astarita A, Palazzo GS, Paradiso V, Squillace A (2015) Microstructural aspects in Al–Cu dissimilar joining by FSW. Inter J Adv Manuf Technol 79:1109–1116. https://doi.org/10.1007/s00170-015-6874-z
28. Saeid T, Abdollah-zadeh A, Sazgari B (2010) Weldability and mechanical properties of dissimilar aluminum–copper lap joints made by friction stir welding. J Alloys Compd 490:652–655. https://doi.org/10.1016/j.jallcom.2009.10.127
29. Regensburg A, Schürer R, Weigl M, Bergmann J (2018) Influence of pin length and electrochemical platings on the mechanical strength and macroscopic defect formation in stationary shoulder friction stir welding of aluminium to copper. Metals, 8. https://doi.org/10.3390/met8020085
30. Avettand-Fènoël M-N, Taillard R, Herbelot C, Imad A (2010) Structure and mechanical properties of friction stirred beads of 6082-T6 Al alloy and pure copper. Mat Sci Forum 638–642:1209–1214. https://doi.org/10.4028/www.scientific.net/MSF.638-642.1209
31. Avettand-Fènoël M-N, Taillard R, Ji G (2012) Quality of interfaces in Cu/Al dissimilar friction-stirred welds. Mat Sci Forum 706–709:959–964. https://doi.org/10.4028/www.scientific.net/MSF.706-709.959
32. Goran D, Avettand-Fènoël M-N, Taillard R (2011) Texture and microstructure evolution in friction stir welded Cu-Al sheets characterized by EBSD. Mat Sci Forum 702–703:574–577. https://doi.org/10.4028/www.scientific.net/MSF.702-703.574
33. Galvão I, Loureiro A, Verdera D, Gesto D, Rodrigues DM (2012) Influence of tool offsetting on the structure and morphology of dissimilar aluminum to copper friction-stir welds. Metall Mater Trans A 43A:5069–5105. https://doi.org/10.1007/s11661-012-1351-x
34. Tan CW, Jiang ZG, Li LQ, Chen YB, Chen XY (2013) Microstructural evolution and mechanical properties of dissimilar Al–Cu joints produced by friction stir welding. Mater & Des 51:466–473. https://doi.org/10.1016/j.matdes.2013.04.056
35. Abdollah-Zadeh A, Saeid T, Sazgari B (2008) Microstructural and mechanical properties of friction stir welded aluminum/copper lap joints. J Alloys Compd 460:535–538. https://doi.org/10.1016/j.jallcom.2007.06.009
36. Galvão I, Verdera D, Gesto D, Loureiro A, Rodrigues DM (2013) Influence of aluminium alloy type on dissimilar friction stir lap welding of aluminium to copper. J Mater Process Technol 213:1920–1928. https://doi.org/10.1016/j.jmatprotec.2013.05.004
37. Galvão I, Loureiro A, Rodrigues DM (2016) Critical review on friction stir welding of aluminium to copper. Sci Technol Weld Join 21:523–546. https://doi.org/10.1080/13621718.2015.1118813
38. Xue P, Xiao BL, Ma ZY (2015) Effect of interfacial microstructure evolution on mechanical properties and fracture behavior of friction stir-welded Al-Cu joints. Metall Mater Trans A 46:3091–3103. https://doi.org/10.1007/s11661-015-2909-1
39. Marstatt R, Krutzlinger M, Luderschmid J, Zaeh MF, Haider F (2017) Formation of a diffusion-based intermetallic interface layer in friction stir welded dissimilar Al-Cu lap joints. IOP Conference Ser: Mater Sci Eng 181:12002. https://doi.org/10.1088/1757-899X/181/1/012002
40. Zhang W, Shen Y, Yan Y, Guo R, Guan W, Guo G (2018) Microstructure characterization and mechanical behavior of dissimilar friction stir welded Al/Cu couple with different joint configurations. Inter J Adv Manuf Technol 94:1021–1030. https://doi.org/10.1007/s00170-017-0961-2
41. Marstatt R, Krutzlinger M, Luderschmid J, Costanzi G, Mueller JFJ, Haider F, Zaeh MF (2018) Intermetallic layers in temperature controlled friction stir welding of dissimilar Al-Cu-joints. IOP Conference Ser: Mater Sci Eng 373:12017. https://doi.org/10.1088/1757-899X/373/1/012017
42. Bachmann A, Gamper J, Krutzlinger M, Zens A, Zaeh MF (2017) Adaptive model-based temperature control in friction stir welding. Inter J Adv Manuf Technol 93:1157–1171. https://doi.org/10.1007/s00170-017-0594-5

43. Yang K, Keat Gan S, Sukkarieh S (2013) A Gaussian process-based RRT planner for the exploration of an unknown and cluttered environment with a UAV. Adv Robot 27:431–443. https://doi.org/10.1080/01691864.2013.756386
44. Schneider M, Ertel W (2010) Robot Learning by Demonstration with local Gaussian process regression. In: 2010 IEEE/RSJ international conference on intelligent robots and systems (IROS), Taipei, Taiwan, October 18–22, 2010. Piscataway Township, USA. 255–260. https://doi.org/10.1109/IROS.2010.5650949
45. Sterling D, Sterling T, Zhang YM, Chen H (2015) Welding Parameter Optimization Based on Gaussian Process Regression Bayesian Optimization Algorithm. In: 2015 IEEE international conference on automation science and engineering (CASE). Gothenburg, Sweden, August 24–28, 2015. Piscataway Township, USA. 1490–1496. https://doi.org/10.1109/CoASE.2015.7294310
46. Dong H, Cong M, Liu Y, Zhang Y, Chen H (2016) Predicting characteristic performance for arc welding process. In: 2016 IEEE international conference on cyber technology in automation, control, and intelligent systems (CYBER). Chengdu, China, June 19–22, 2016. Piscataway Township, USA. 7–12. https://doi.org/10.1109/CYBER.2016.7574786
47. Dong H, Cong M, Zhang Y, Liu Y, Chen H (2018) Modeling and real-time prediction for complex welding process based on weld pool. Inter J Adv Manuf Technol 86. https://doi.org/10.1007/s00170-018-1685-7
48. Goodfellow I, Bengio Y, Courville A (2016) Deep learning. MIT Press, Cambridge, p 0262035618
49. Bishop CM (2009) Pattern recognition and machine learning, 8th edn. Springer, New York, p 0387310738
50. Snelson EL (2007) Flexible and efficient Gaussian process models for machine learning. University College London, Dissertation
51. Rasmussen CE, Williams CKI (2006) Gaussian processes for machine learning, 3rd edn. MIT Press, Cambridge, p 026218 253X
52. Duvenaud DK (2014) Automatic model construction with gaussian processes. University of Cambridge, Dissertation
53. Park K, Paulino GH (2011) Cohesive zone models: A critical review of traction-separation relationships across fracture surfaces. Appl. Mech. Rev 64(6):60802-1–60802-20. https://doi.org/10.1115/1.4023110
54. Casalino G, Guglielmi P, Lorusso VD, Mortello M, Peyre P, Sorgente D (2017) Laser offset welding of AZ31B magnesium alloy to 316 stainless steel. J. Mater. Proc. Techn. 242:49–59. https://doi.org/10.1016/j.jmatprotec.2016.11.020

Affiliations

M. Krutzlinger[1] · E. Meltzer[1] · M. Muehlegg[2] · M. F. Zaeh[1]

E. Meltzer
elias.meltzer@tum.de

M. Muehlegg
maximilian.muehlegg@tum.de

M. F. Zaeh
michael.zaeh@iwb.mw.tum.de

[1] Institute for Machine Tools and Industrial Management, Technical University of Munich (TUM), Boltzmannstrasse 15, 85748 Garching, Germany

[2] Institute of Flight System Dynamics, Technical University of Munich (TUM), Boltzmannstrasse 15, 85748 Garching, Germany